

ENHANCEMENT AND DEGRADATION: THE DUAL ROLE OF GRAPHENE NANOPLATELETS ON THE STRUCTURAL PERFORMANCE OF COMPOSITE T-JOINTS AND MECHANISTIC INSIGHTS

Mukesh Bhasin[1], Adrian Mouritz[1]

[1]School of Engineering, RMIT University, Melbourne, Australia

Abstract

This paper reports an experimental investigation into the effect of graphene nanoplatelet (GNP) inclusion on the structural properties of carbon-epoxy T-joints under stiffener pull-off loading. T-joints with 0.0–2.0 wt.% GNPs (five concentrations; ≥9 specimens each) were tested. GNP addition significantly improved toughness-reliant properties: load drop after damage initiation reduced by up to 93%, absorbed energy capacity increased by up to 17%, and fracture propagation transformed from unstable stick-slip to stable distributed cracking. DIC characterisation revealed progressive strain field diffusion with GNP content. Conversely, joint stiffness decreased by up to 36%, damage initiation load by up to 24%, and ultimate strength by up to 25% at high GNP concentrations. The study identifies the effective dispersion window for balanced performance. Mechanisms responsible for both enhancement and degradation are identified and linked not only to continuum mechanics scale factors but also at the quantum mechanical forces scale. This study yields two pivotal insights: (a) the filler–matrix interface emerges as the true performance ceiling and primary design lever for T-joint composites, (b) graphene's reinforcement potential hinges on de-stacking GNPs into individual monolayers due to the weak van der Waals interlayer properties—a perspective that supersedes the conventional dispersion–agglomeration phenomenological model treating platelets as intact multi-layer units.

Keywords: Graphene nanoplatelets; Carbon/epoxy composites; T-joints; Damage tolerance; DIC; Aerospace structures

1. INTRODUCTION

T-joints are critical load-bearing connections in aircraft and spacecraft structures [1-3], appearing at bulkhead/fuselage-skin, rib-skin and spar-skin junctions where they resist bending and transfer loads in thin-walled panels [4, 5]. Comprising a web, flange and deltoid fillet, the joint must transfer laminate's in-plane fibre loads through the inherently weaker through-thickness direction [6]. It is known that T-joint damage initiates at the radius bend due to geometric stress concentration and progresses by delamination governed by mixed mode I and mode I/II fracture toughness [7].

Despite extensive research on GNPs in composite laminates, their effect on structural performance of actual structural elements such as T-joint is almost entirely uncharacterized. Only one computational study [8] and one nanofibres-placement patent [9] exist, neither accounting for scaled manufacturing dependent complexities. This paper reports the first systematic experimental study of GNP effects on composite T-joint structural properties, identifies the governing mechanisms, and establishes the effective concentration window for net structural benefit.

This study is limited to one joint geometry (T-joint) and material configuration (15-ply plain woven CFRP), quasi-static pull-off loading, and one GNP type (xGNP M-25) processed by three-roll mill calendaring without solvent or surfactant use. For most specimens, results were reproducible across

independently fabricated specimens within each GNP loading level, as reflected by the tight clustering of data points around the group means. Generalisation to combination of other geometries and loading modes (fatigue, impact, compression), or GNP types requires further investigation.

2. MATERIALS AND METHODOLOGY

2.1 Fabrication of GNP-Reinforced T-Joints

15 ply carbon T-joints were fabricated from 198 gsm plain woven 3K carbon fabric (Colan Ltd) with West System 105/206 bisphenol-A epoxy (tensile modulus: 3.17 GPa; tensile strength 50.5 MPa flexural modulus: 3.10 GPa, Flexural strength: 81.4 MPa; mix viscosity: 725 cP at 22°C) [10, 11]. GNPs (xGNP M-25, XG Sciences; lateral dimension: 25 μm, thickness: 6–8 nm, surface area: 120–150 m^2/g) [12, 13] were incorporated at 0, 0.5, 1.0, 1.5 and 2.0 wt.%. Dispersion was by six-pass three-roll mill calendaring (final conditions: 150 rpm, 20 μm gap; no solvent). T-joints were assembled in a machined aluminium mould, vacuum-bag consolidated and room-temperature cured for four days. Figure 1 illustrates the fabrication sequence.

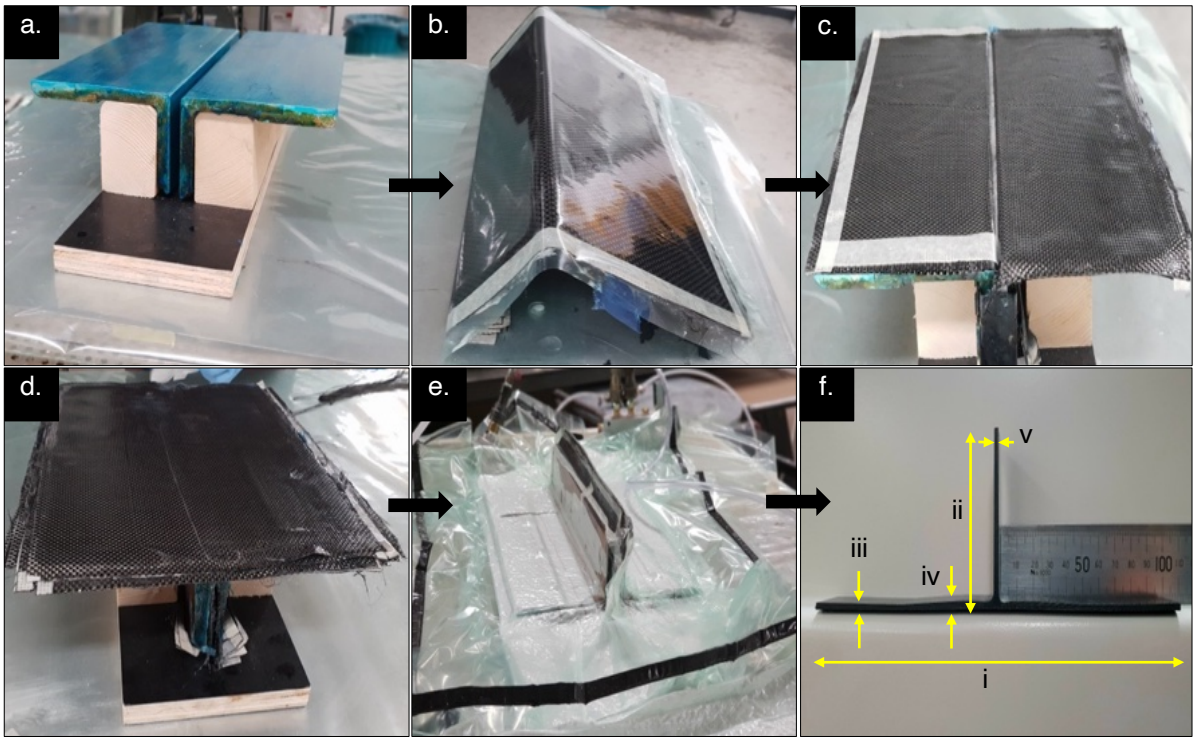
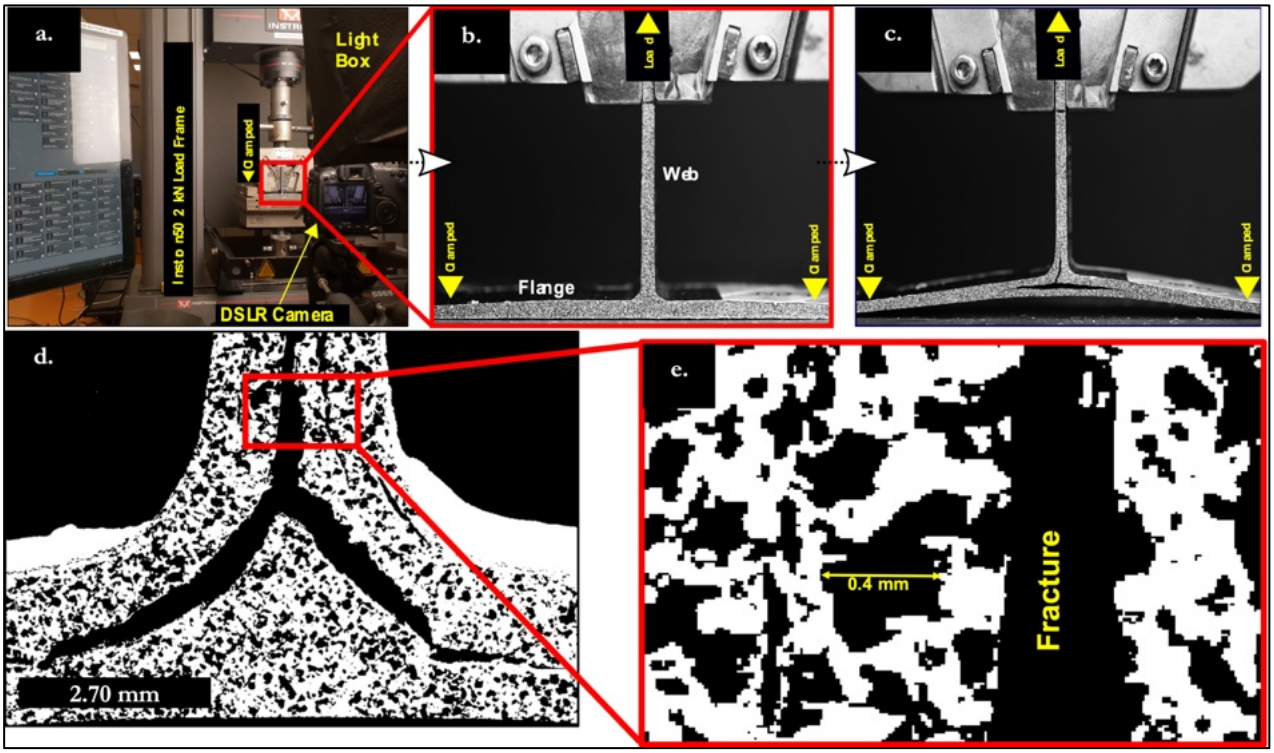


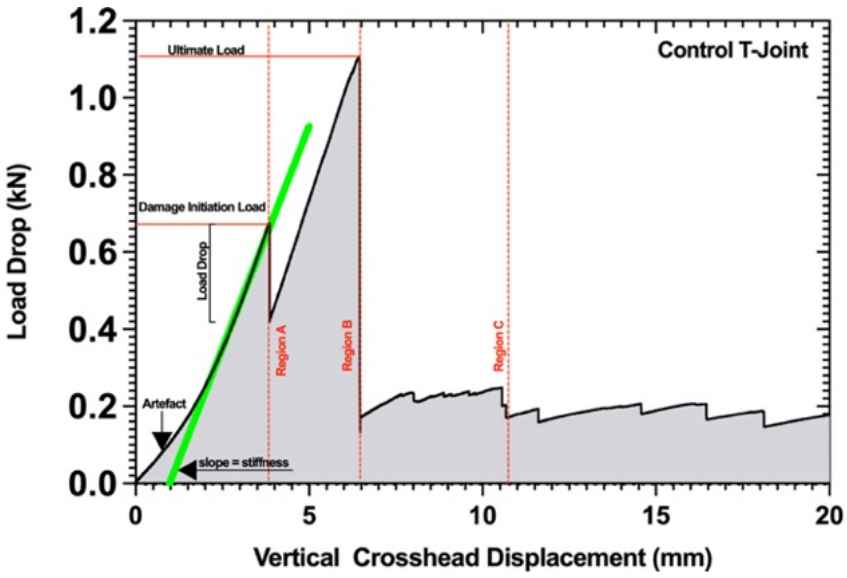
Figure 1 – Fabrication methodology: a. aluminium mould with PVA release film, b. 5-ply wet hand layup on each L-section with 32 3k filament tows placed in Δ-fillet, c. assembled and clamped L-sections with 5-ply laminate, d. 5-ply overlaminate flange, e. vacuum consolidation, f. Specimen dimensions: (*i*) 200 mm, (*ii*) 70 mm (*iii*) 2.7 mm (*iv*) 3.50 mm (*v*) ca. 2.7 mm.

2.2 Stiffener Pull-Off Testing and DIC

Stiffener pull-off tests were performed on an Instron 5569 (crosshead rate: 2 mm/min; total displacement: 30 mm; ≥9 specimens per type) with flange ends clamped to a custom steel support [See Figure 2 (i) b., c.)]. Structural properties extracted include joint stiffness (Region A slope in Figure 2 (ii)], damage initiation load (first load drop), load drop magnitude, ultimate load, displacements at both events, and absorbed energy capacity (AEC = area under load-displacement curve). Statistical significance was assessed using ANOVA with Šídák correction. All results are presented as mean ± SEM; individual specimen data points are shown to illustrate within-group variability. Full-field Green-Lagrangian surface strains (ε_{xx}, ε_{xy}, ε_{yy}) were measured by Digital Image Correlation (using Ncorr MATLAB; Canon EOS 50D camera with1 frame/s; while assuring speckle dot diameter <0.4 mm).



(i)



(ii)

Figure 2 – (i)a: Stiffener pull-off test configuration, specimen states at (i)b: Test commencement and (i)c: Test conclusion, (i)d: and (i)e: Magnified DIC speckle pattern, and (ii) Neat specimen baseline reference showing three-region load-displacement response (Region A: elastic, captures damage initiation load; B: elastic, captures ultimate load; C: failure progression through web/flange through delamination).

3. RESULTS AND DISCUSSION

The results are presented in order of the novelty, magnitude of the GNP effect and importance to aerospace primes/OEM (Original Equipment Manufacturer) and operators of aeronautical and astronautical systems, from the most significant to the least.

3.1 Load Drop after Damage Initiation — Most Significant Enhancement

Load drop magnitude after initiation and stable fracture progression (determined through DIC enabled crack length & branching measurement) is of high importance to primes as it reveals post-damage structural behaviour and influences residual structural strength capability and is needed by aerospace

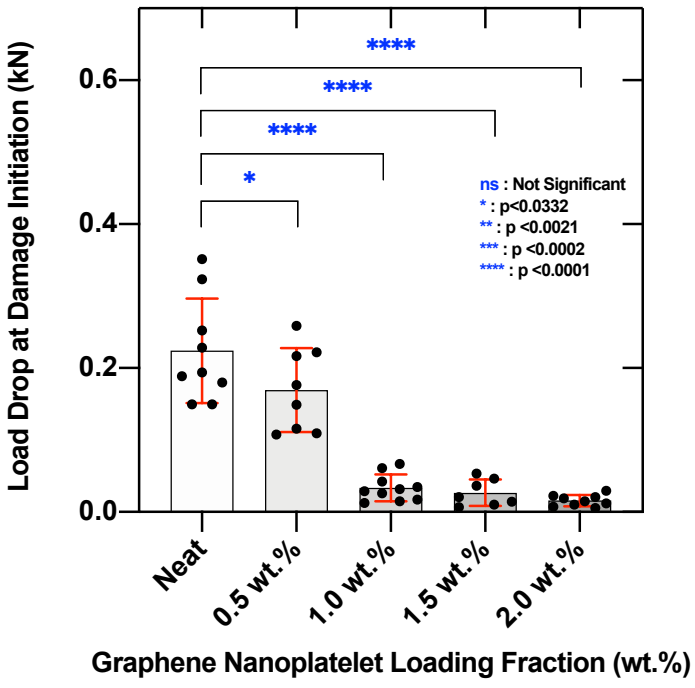
primes for certification of bonded primary structures. Its importance to operators is also high as it affects damage spread speed and helps with assessment of whether damage is “inspectable and/or stable” as operators need predictable, slow, stable cracking for safe continued flight.

The results show that the most dramatic and consistently beneficial effect of GNP addition was a monotonic, statistically significant reduction in load drop at damage initiation [Table 1; Figure 3 (a)]. At 0.5 wt.% the load drop reduced by 24%; at 1.0 wt.% by 85%; and at 2.0 wt.% by 93% (from 0.224 N to 0.016 N). All reductions from 0.5 wt.% onward were statistically significant ($p \leq 0.04$). Fractographic images [Figure 3 (b)] confirm the transformation from a single abrupt crack (row 1 and 2: unmodified; 0.5 wt.%) to many small simultaneously advancing cracks (row 3-5: 1.0–2.0 wt.%).

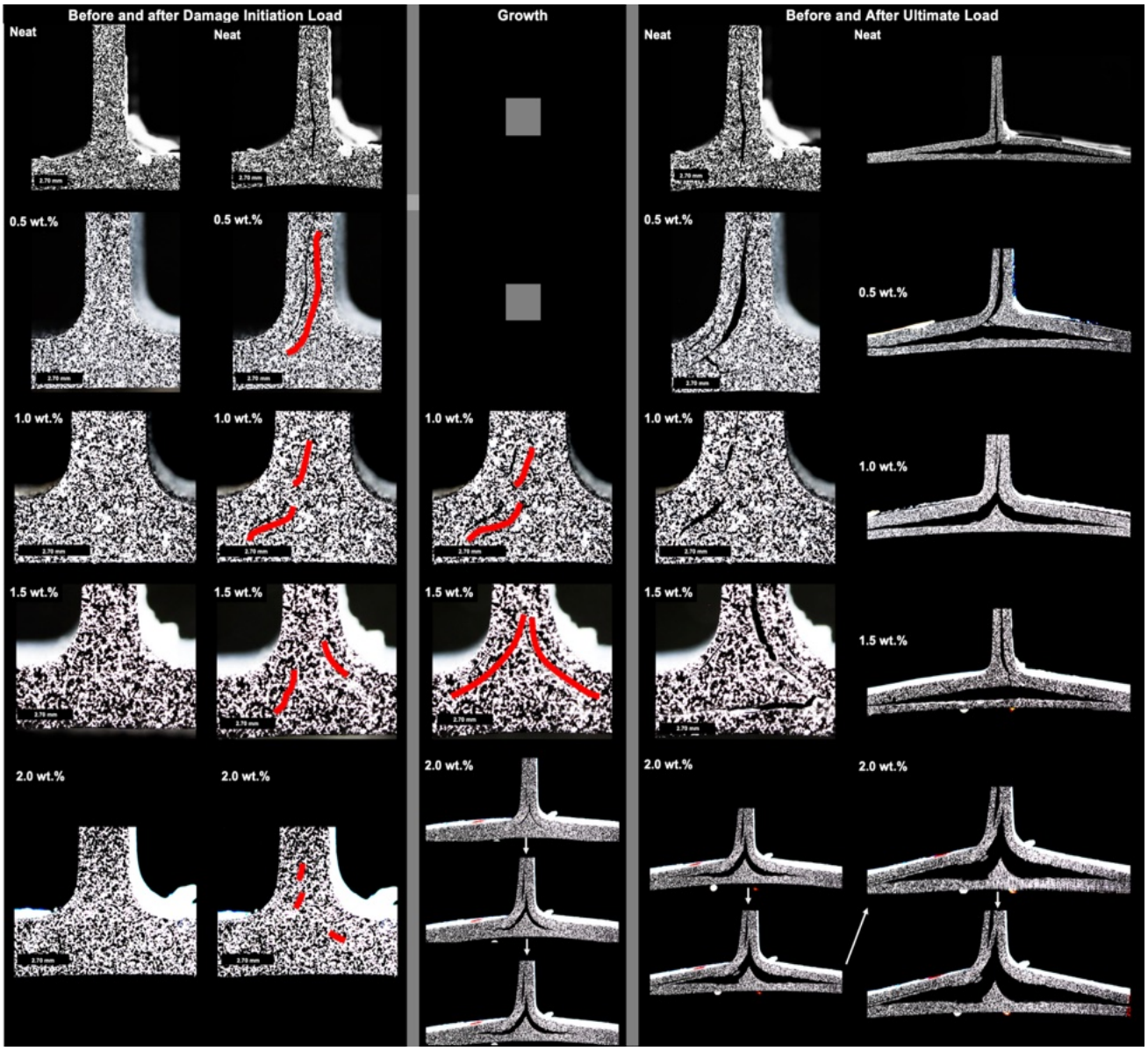
Mechanisms: The experimental findings along with fractography suggest that GNPs activate multiple concurrent toughening mechanisms at the fracture process zone spanning, not only continuum mechanics scale, but also at the scale of intramolecular quantum mechanical forces: with (a) crack deflection and branching at GNP–matrix interfaces; (b) graphene–matrix debonding (~0.4 MPa interfacial shear strength) [14]; (c) frictional sliding between graphene layers falling in first category; and (d) interlayer graphene separation (consuming interlayer binding energy 0.15–0.34 J/m^2 per unit graphene–graphene area) [15], falling in the latter category. These mechanisms collectively redistribute fracture energy over a larger spatial and temporal extent, suppressing the sudden load release characteristic of unstable crack initiation.

Table 1 – Load drop at damage initiation (ANOVA Šídák correction; ≥9 specimens per type).

Specimen	Load Drop (N)	% Change	P-Value	Significant
Unmodified	0.224 (SD:0.073)	–	–	–
0.5 wt.%	0.170 (SD:0.060)	−24%	0.04	Yes
1.0 wt.%	0.033 (SD:0.020)	−85%	<0.0001	Yes
1.5 wt.%	0.027 (SD:0.020)	−88%	<0.0001	Yes
2.0 wt.%	0.016 (SD:0.008)	−93%	<0.0001	Yes



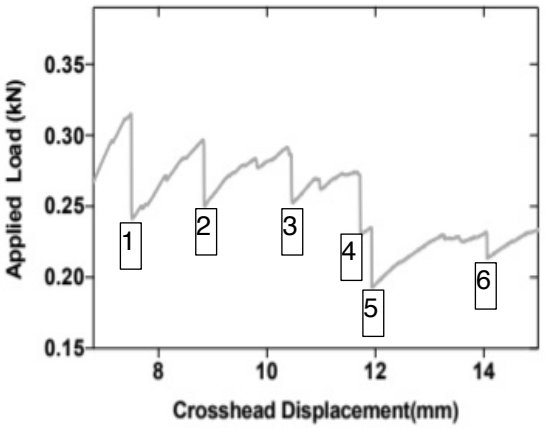
(a)



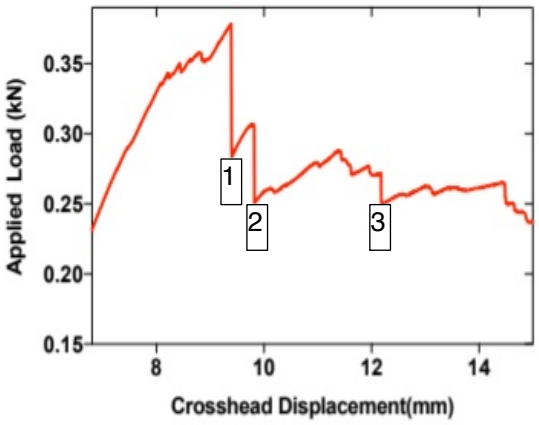
(b)

Figure 3 – (a) Load drop vs. GNP content: significant reductions from 0.5 wt.%. (b) Damage evolution images for all joint types before/after damage initiation and before/after ultimate load (fractures red). Single-crack (for 0-0.5 wt.%) to multi-crack transformation (for 1-2 wt.%).

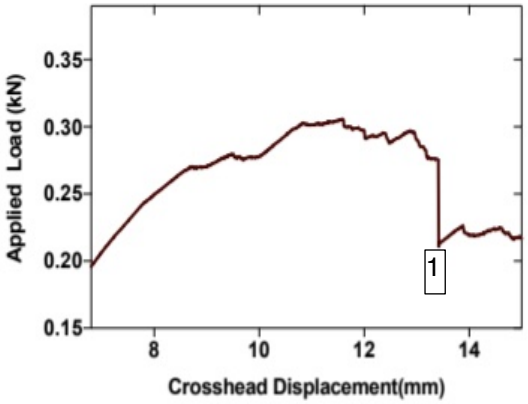
Fracture propagation [Region B to C of Figure 2 (ii)] above also showed a marked GNP effect (Figure 4). The unmodified joint exhibited a clear saw-tooth load-displacement response with 6 load drops >0.015 kN (diagnostic of stick-slip unstable crack propagation). The 2.0 wt.% specimen showed only 1 such drop, confirming globally stabilised crack growth sustained well beyond the ultimate load. DIC confirmed that higher GNP concentrations shift fracture energy dissipation from mode II web fracture to mode I flange fracture consistent with GNPs improving mode I, but not mode II fracture toughness [16-20].



(a)



(b)



(c)

Figure 4 – Region C (post-peak) load-displacement curves for (a) unmodified, (b) 1.0 wt.% and (c) 2.0 wt.% GNP joints. Saw-tooth stick-slip (a) transitions to smooth stable propagation (c).

3.2 Absorbed Energy Capacity

Absorbed Energy Capacity (AEC) is critical on two fronts. For OEMs, it is a cornerstone of static crashworthiness substantiation and certification, as higher AEC translates directly to superior crash energy management. For operators, it delivers tangible value: greater energy absorption means greater tolerance for impacts and overloads in real-world scenarios, reducing maintenance costs and downtime when crashes or overloads occur.

The results (Figure 5, Table 2) show that on 1.0 wt. % GNP addition, AEC improved significantly at 0.5 wt.% (+14%; p=0.014) and 1.0 wt.% (+17%; p=0.014; Table 2). Despite AEC's bimodal scatter from dispersion variability, 0.5 and 1.0 wt.% means remain significantly elevated ($p < 0.0332$). Above 1.0 wt.%, AEC returned to near-baseline (–4% at 1.5 wt.%, +1% at 2.0 wt.%; both statistically insignificant). The optimum at 1.0 wt.%, rather than the 1.5 wt.% observed in companion flat-panel fracture toughness tests [17] is attributed to intensified filtration-induced re-agglomeration at ply interfaces during vacuum consolidation, which depletes the effective toughening volume at higher concentrations.

Mechanisms: Mechanisms by which AEC improved is driven by GNP-enhanced mode I interlaminar toughness, which increases total fracture surface area through crack bifurcation and deflection [17] throughout the entire damage history including post-peak Region C in Figure 2 (ii).

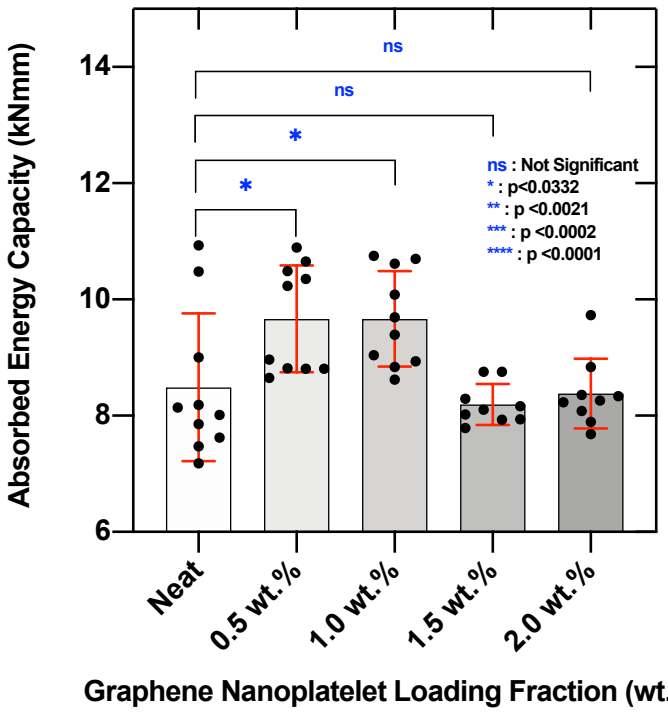


Figure 5 – Absorbed energy capacity: peak at 1.0 wt.% before filtration-induced re-agglomeration dominates.

Table 2 – Absorbed Energy Capacity.

Specimen	AEC (kN·mm)	% Change	P-Value	Sig.
Unmodified	8.49 (SD:1.27)	–	–	–
0.5 wt.%	9.67 (SD:0.92)	+14%	0.014	Yes
1.0 wt.%	9.97 (SD:0.82)	+17%	0.014	Yes
1.5 wt.%	8.19 (SD:0.35)	−4%	0.9	No
2.0 wt.%	8.38 (SD:0.60)	+1%	1.0	No

3.3 DIC Strain Field Characterisation

DIC characterisation is of modest relevance to OEM and operators but is extremely valuable research tool for mechanistic insight. In the present study, DIC at damage initiation revealed progressive transformation of the strain field from concentrated-localised to diffuse-distributed with increasing GNP content (Figure 6). In the unmodified joint, the ε_{xx} strain field was highly localised at the deltoid bend, with the high strain contour sharply defining the impending fracture plane. At 2.0 wt.%, the high-strain contour was nearly absent, with strain distributed over the entire deltoid region. Quantitatively, strain field tensile maxima (Table 3) decreased monotonically with GNP content across all strain components (ε_{xx} tension slope m=–0.02; ε_{xy} shear slope m=–0.002; ε_{yy} compressive slope m=–0.004), while compressive extrema showed modest corresponding reductions. The modest compressive-extrema slopes ($|m| \approx 0.005$) relative to the dominant tensile response ($|m| = 0.02$ for $\varepsilon_{xx,tension}$) reflect two converging constraints, limited by both (a) an incomplete activation of GNP toughening mechanisms and, (b) the intrinsically small compressive strains imposed by the loading geometry. First, kinematically, the stiffener pull-off geometry produces a predominantly tensile field at the deltoid fillet, with compressive strains arising only as secondary reactions an order of magnitude smaller than the tensile extrema ($\varepsilon_{xx,comp} = -0.01$ vs $\varepsilon_{xx,tension} = +0.08$), thereby bounding the achievable reduction. Second, mechanistically, the principal GNP energy-dissipation pathways—interfacial debonding, platelet pull-out, crack deflection, and interlayer slip—are inherently opening-mode processes that require surface separation or shear translation. Under compression, these pathways are suppressed as gaps close and elevated normal pressure inhibits inter-layer slippage.

Mechanisms: Key mechanisms leading to the identified behaviour are as follows: (a) The strain diffusion reflects redistribution of crack-tip stress concentration energy across a broader fracture process zone. (b) GNPs also introduce concurrent energy sinks: (b.1) interlayer shear and separation (interlayer binding energy 0.15–0.34 J/m^2) [21-23], (b.2) graphene–matrix debonding and friction preventing strain localisation. Also, at high GNP concentrations, early micro-damage from intra-resin GNP disconnection (attributable to weak vdW bonds and low ~ 0.4 MPa interfacial shear strength) [14, 24] dissipates fracture energy before formation of a dominant crack front.

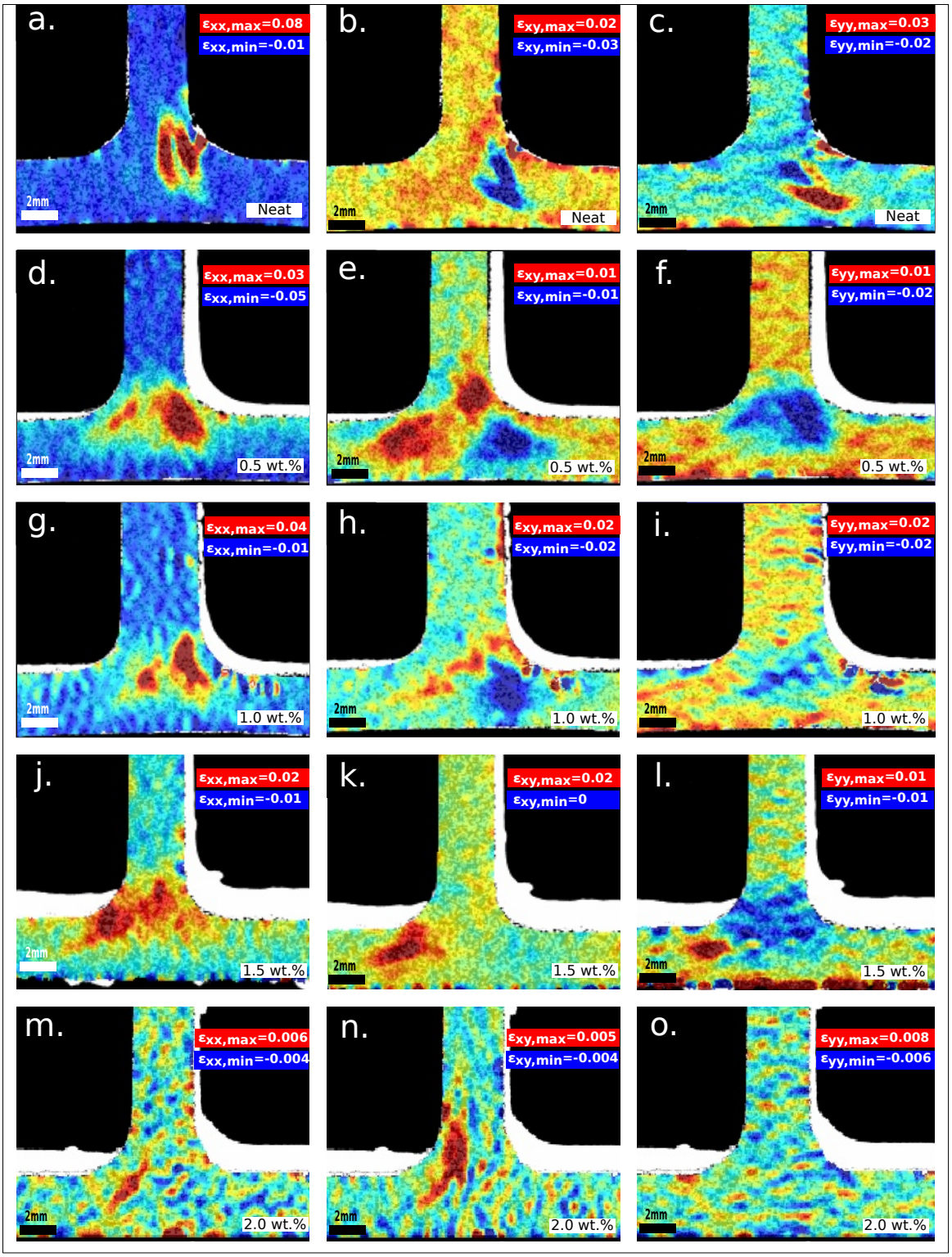


Figure 6 – DIC strain heatmaps before damage initiation (rows: 0–2.0 wt.%; columns: ε_{xx}, ε_{xy}, ε_{yy}). High-strain zone transitions from concentrated (0 wt.%) to diffuse (2.0 wt.%), evidencing a broader fracture process zone.

Table 3 – Green-Lagrangian strain field extrema at damage initiation (trend slope ***m*** over GNP concentration).

Specimen	ε_{xx} (ten)	ε_{xy} (ten)	ε_{yy} (ten)	ε_{xx} (comp)	ε_{xy} (comp)	ε_{yy} (comp)
Unmodified	0.08	0.02	0.03	−0.01	−0.03	−0.02
0.5 wt.%	0.03	0.01	0.005	−0.05	−0.01	−0.02
1.0 wt.%	0.04	0.02	0.02	−0.01	−0.02	−0.02
1.5 wt.%	0.02	0.02	0.01	−0.01	0	0
2.0 wt.%	0.006	0.005	0.008	−0.004	−0.004	−0.006
Slope (m)	−0.020	−0.002	−0.004	+0.005	+0.006	+0.005

3.4 Damage Initiation Load and Ultimate Strength

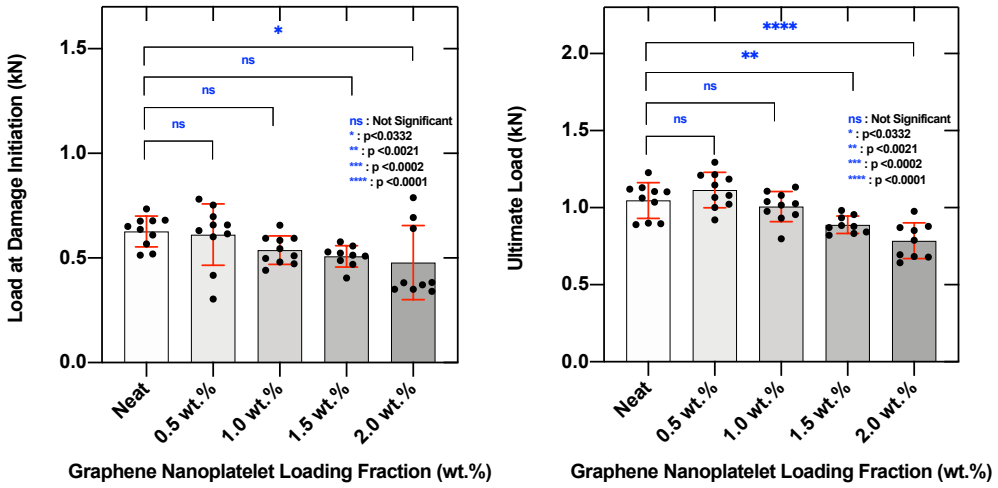
The damage initiation load is extremely important for both OEMs and operators. For OEMs it sets the threshold for no-growth or slow-growth damage tolerance — a concept core to composite damage tolerance philosophy (AC 20-107B) [25, 26]. Criticality to operators for this property is also very high as it defines initiation of detectable damage, thus defining inspection intervals as lower initiation load signifies earlier maintenance.

Results show that on addition of GNP to the composite T-Joints, damage initiation load showed a statistically significant reduction only at 2.0 wt.% (–24%; p=0.02); with all other changes being insignificant (Table 4, Figure 7). Ultimate load was insignificantly altered at ≤1.0 wt.% (mean +6% at 0.5 wt.%; –4% at 1.0 wt.%) but showed significant reductions of 15% at 1.5 wt.% and 25% at 2.0 wt.% (both p≤0.007; Table 4).

Mechanisms: The monotonic decrease in both properties is attributed to the fact that above ~0.5–1.0 wt.%, GNP agglomerates function as equivalent flaw regions, concentrating stress and triggering premature failure, overwhelming the reinforcing effect of isolated dispersed platelets.

Table 4 – Damage initiation load and ultimate load (all concentrations).

Specimen	Dmg Init (kN)	%	p-val	Ult. Load (kN)	%	p-val	Sig.
Unmodified	0.627 (0.073)	–	–	1.05 (0.12)	–	–	–
0.5 wt.%	0.612 (0.147)	−2%	1.0	1.11 (0.12)	+6%	0.40	No
1.0 wt.%	0.538 (0.068)	−14%	0.3	1.01 (0.10)	−4%	0.80	No
1.5 wt.%	0.508 (0.051)	−19%	0.1	0.89 (0.06)	−15%	0.007	Yes
2.0 wt.%	0.478 (0.177)	−24%	0.02	0.79 (0.12)	−25%	<0.0001	Yes



(a) (b)

Figure 7 – (a) Damage initiation load: significant reduction at 2.0 wt.% only. (b) Ultimate load: significant reductions above 1.0 wt.%.

3.5 Joint Stiffness

Stiffness is an essential airframe design requirement. Its criticality to OEM is high, as it is required for aeroelasticity, buckling prevention, and deflection limit assessment. Joint stiffness is also prioritised by operators over other service critical attributes of strength and damage tolerance as it critically affects structural deflection, causing vibration and fatigue damage.

Experimental results in the present study show that joint stiffness magnitude decreased monotonically with GNP content increase, from a statistically insignificant –4% at 0.5 wt.% to a significant –36% at 2.0 wt.% (Table 5, Figure 8), suggesting a concentration-dependent degradation mechanism,

superseding any stochastic scatter. The evidence collectively indicates that stiffness peak lies below 0.5 wt.%, consistent with meta-analysis of 32 nanocomposite stiffness datasets [27], in which peak stiffness occurred at ≤1.0 wt.% in 64% of studies, with agglomeration identified as the root cause of subsequent decline in virtually all cases [28].

Table 5 – Joint stiffness.

Specimen	Stiffness (kN/mm)	% Change	P-Value	Significant
Unmodified	0.209 (SD:0.14)	–	–	–
0.5 wt.%	0.201 (SD:0.012)	−4%	0.882	No
1.0 wt.%	0.175 (SD:0.018)	−16%	0.0054	Yes
1.5 wt.%	0.153 (SD:0.030)	−27%	<0.0001	Yes
2.0 wt.%	0.134 (SD:0.020)	−36%	<0.0001	Yes

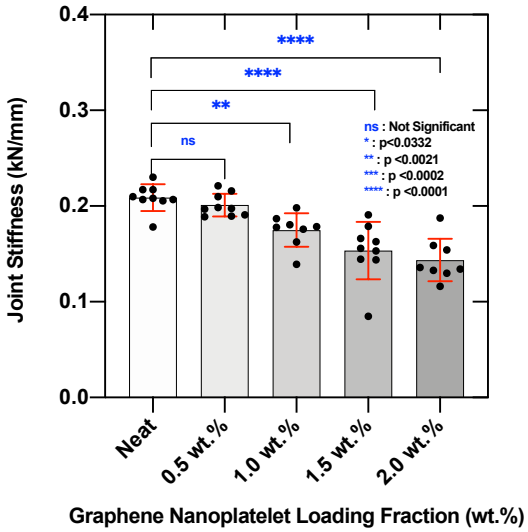


Figure 8 – Joint stiffness vs. GNP content: Monotonic significant decrease from 1.0 wt.%. Stiffness peak lies below 0.5 wt.%.

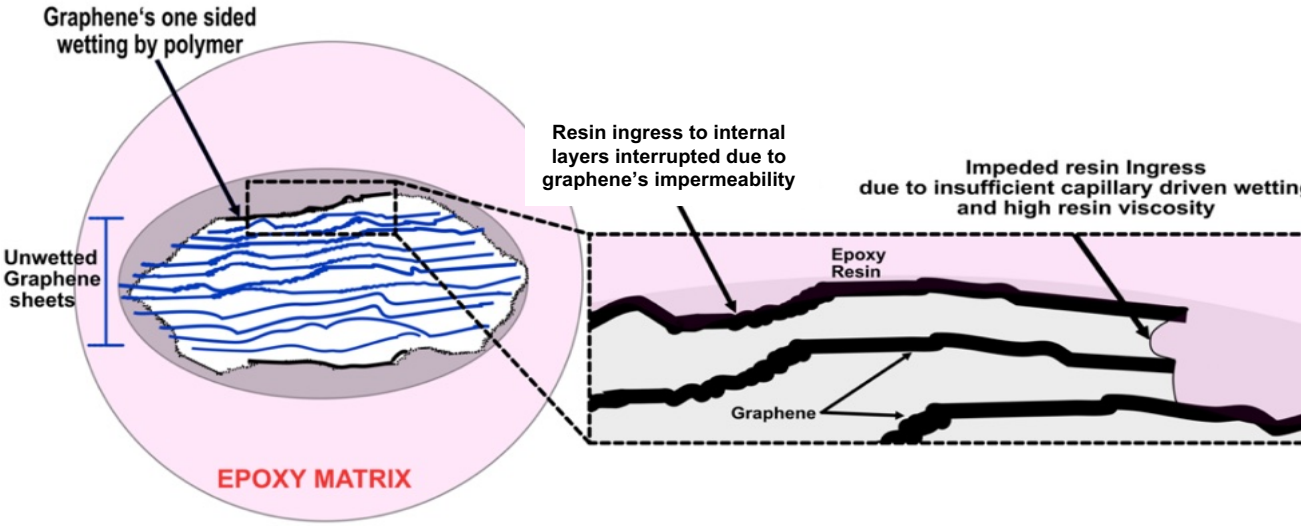
Mechanisms: Three coupled mechanisms are responsible for stiffness reduction:

(i) *Retained multilayer platelet architecture*: The three-roll mill calendaring reduced agglomerate size but did not separate individual graphene layers. Unexfoliated GNPs contribute stiffness only through peripheral layers in contact with the matrix, resulting in loss of potential graphene-matrix interfacial area; the internal layers transfer stress only via weak vdW interlayer bonds [14]—corresponding to out-of-plane modulus $C_{33} \approx 38$ GPa [22, 29, 30] and shear modulus (C_{44}) ≤ 5 GPa for AB Bernal-stacked graphene [30-36], C_{44} as low as 0.13 GPa for turbostratic stacking [29, 32], and 3.8 GPa for AA stacked GNP [32] which is far below graphene's in-plane 1 TPa [21, 37]. The disparity between these values and graphene's in-plane modulus spanning two to four orders of magnitude confirms that unexfoliated GNPs constitute a stiffness liability within the matrix rather than a reinforcement, since each platelet introduces a mechanically weak inclusion in place of the epoxy volume it displaces.

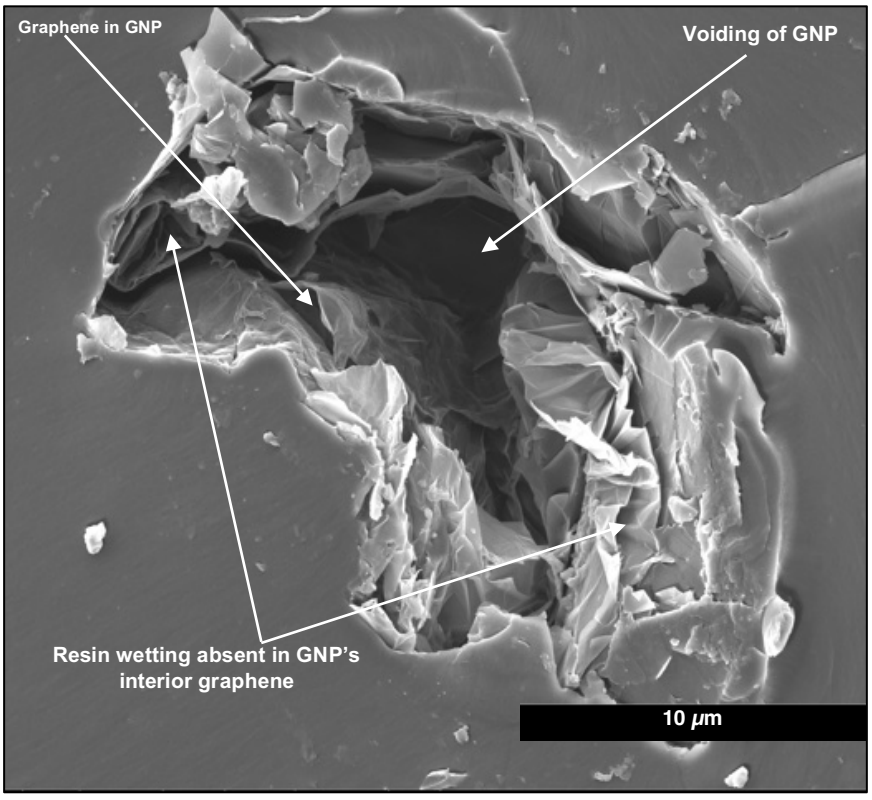
(ii) *Filtration induced clustering*: As shown in Figure 9 (c), GNPs accumulated in fibre tow cross-pockets during wet layup and concentrated at the vacuum bag filtration interface during consolidation (evidenced by GNP-free expelled resin and clogged release film pinholes), creating macro-scale agglomerates [elongated inter-fibre tow bands (red outlines) and cross-pocket clusters (black arrows)] that function as "equivalent flaw regions" reducing effective modulus. SEM confirmed increasing agglomerate density with GNP content.

(iii) *vdW interstice displacement*: Within each xGNP M-25 platelet (~18–20 graphene layers), carbon atoms occupy ~ 50 vol.% while the remainder is low-stiffness vdW interstice. Each GNP therefore displaces an equivalent volume of epoxy with vdW space, directly reducing the effective matrix modulus. As illustrated in Figure 9(a) and confirmed by the interior voiding

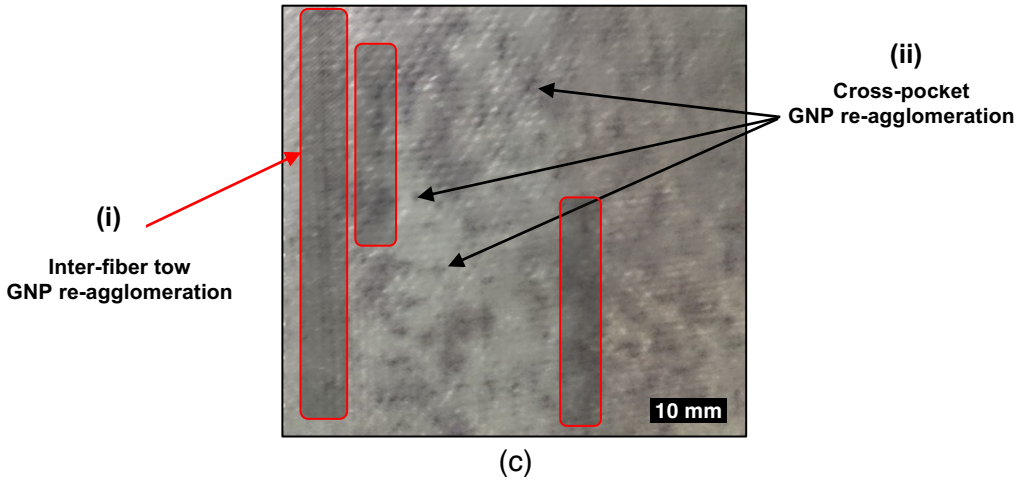
visible in Figure 9(b), high resin viscosity and graphene's impermeability prevent matrix penetration of the interlayer space.



(a)



(b)

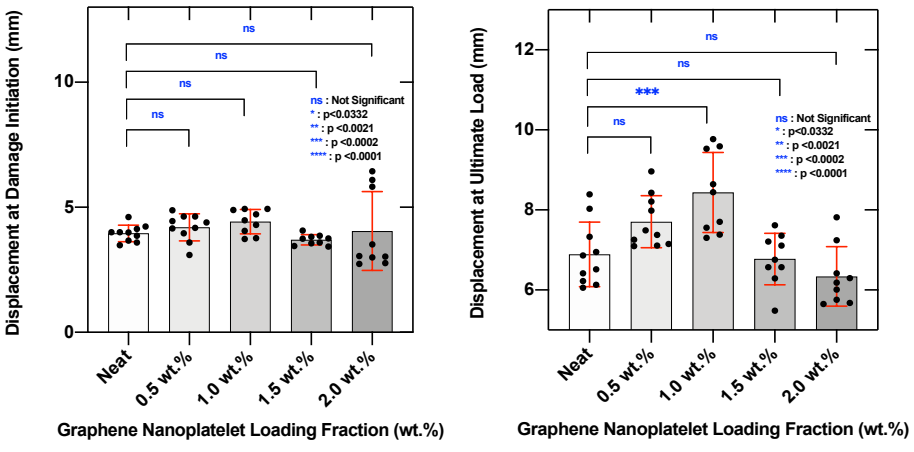


(c)

Figure 9 – (a) Schematic representation, and (b) SEM micrograph of a graphene nanoplatelet (GNP) within an epoxy matrix, illustrating one-sided polymer wetting of the exterior and un-wetted internal graphene sheets, with interior voiding attributed to graphene's impermeability, insufficient capillary-driven wetting, and high resin viscosity, (c) Optical image of a GNP-doped composite laminate illustrating GNP re-agglomeration in two distinct regions: (i) elongated inter-fiber tow bands (red outlines) and (ii) dispersed cross-pocket clusters within the resin-rich inter-tow regions (black arrows).

3.6 Failure Displacements

Failure displacements are not the sole certification driver, but inform deformation limits and design margins for OEMs, and is of practical importance as visible deformation warning to operators. In this context, the experimental results showed that GNP addition had no statistically significant effect on displacement at damage initiation across all concentrations (range: 3.5–5.0 mm) (Figure 10). At ultimate load, a statistically significant 23% increase was measured only at 1.0 wt.% (8.44 mm vs. 6.89 mm; p=0.0004); all other changes being insignificant. These findings confirm that GNPs at 1 wt.% loading primarily modified fracture energy rather than the deformation thresholds at which critical structural events occur, thus acting more as process-zone modifiers rather than stiffness enhancers.



(a) (b)

Displacement at Damage Initiation					Displacement at Ultimate Load			
Specimen Type	Displacement (mm)	% Change	P-Value	Significant	Displacement (mm)	% Change	P-Value	Significant
Unmodified	3.958 (SD:0.0331)	-	-		6.891 (SD: 0.805)	-	-	
0.5 wt.%	4.197 (SD:0.538)	6	1.0	No	7.706 (SD: 0.652)	12	0.08	No
1.0 wt.%	4.422 (SD:0.5)	12	0.5	No	8.44 (SD: 1.003)	23	0.0004	Yes
1.5 wt.%	3.698 (SD: 0.21)	-7	1.0	No	6.774 (SD: 0.646)	-2	1.0	No
2.0 wt.%	4.049 (SD: 1.576)	2	1.0	No	6.340 (SD: 0.741)	-8	0.360	No

(c)

Figure 10 – Displacements at (a) damage initiation and (b) ultimate load for unmodified and GNP doped (0.5 wt.%, 1.0 wt.%, 1.5 wt.% and 2.0 wt.%) T-joints, (c) Results table with test of significance values for all specimens.

3.7 Mult-scale Mechanistic Insights and Failure Hierarchy: From Atomistic Properties to Micromechanical Response and GNP T-joint Structural Performance.

Overall the results demonstrate that the mechanical response of graphene nanoplatelet (GNP) T-joint composites is substantively governed by a small set of well-defined constitutive atomistic properties that span four orders of magnitude in stiffness and strength. Understanding of and disentangling them from effective microstructural bulk properties is essential for interpreting deformation and failure in these systems at macroscale. These are described below as:

1. Interlayer binding energy (0.15–0.34 J/m²) (Cleavage energy budget): The irreversible energy per area to peel two graphene layers apart spent in all cases when interlayer contact fully breaks.
2. C_{33} ≈ 38 GPa (Out-of-plane normal stiffness): Reversible c-axis elastic stiffness, ~25× less stiff than graphene's in-plane response.
3. C_{44} (≤5 / 0.13 / 3.8 GPa)(Interlayer shear stiffness): Elastic shear resistance between layers, reducible from ~5 GPa (AB Bernal) to ~0.13 GPa (turbostratic) as interlayer registry is lost.
4. In-plane modulus ~1 TPa (In-plane covalent bond stiffness): The sp² in-plane reference revealing graphene's up-to-8000× mechanical anisotropy.
5. Graphene–matrix interfacial shear strength (~0.4 MPa)(Interface debonding threshold): Failure stress for flake-to-matrix slip, which is orders of magnitude weaker than any interlayer property, and the first link to break in a composite.

These five properties, spanning 0.4 MPa to 1 TPa, therefore dictates the failure hierarchy governing graphene T-joint composites deformation, fracture and rupture. Under load, the graphene/polymer composite first fails sequentially along its weakest link: (i) the graphene–matrix interface debonding first at ~0.4 MPa, the lowest-strength feature; (ii) interlayer shear and delamination follow, governed elastically by C_{44} — especially in turbostratic flakes — and energetically bounded by the 0.15–0.34 J/m² binding energy; (iii) in-plane fracture of graphene itself, with its ~1 TPa stiffness and ~100 GPa strength, is approached at far higher rarely reached stresses in practice. Thus the 0.4 MPa interfacial strength [roughly *four orders of magnitude* below even the weakest interlayer shear modulus (0.13 GPa = 130 MPa) and ~9 orders of magnitude below in-plane stiffness] sets the first-failure threshold, C_{33} and C_{44} govern the elastic response leading up to it, the binding energy caps interlayer separation, and the in-plane 1 TPa stiffness limit specifies the anisotropic deformation, thus establishing the filler–matrix interface, not graphene itself, as the operative limit and decisive design lever for real-world composite T-joint performance.

4. CONCLUSIONS

This research identifies the precise mechanisms and conditions through which GNPs effect properties of a realistic composite T-joint structures. By establishing concentration as a primary design parameter, the study elucidates the governing constitutive (atomistic) and effective (micromechanical) reinforcement mechanisms, establishing a rigorous basis for the structural application of graphene nanocomposites. The identification of structural properties that experienced detrimental impacts provides critical boundary constraints for subsequent developments. Based on these, the following six principal findings characterise the influence of 1 wt.% GNP content on the structural response of composite T-joints:

1. **Reduced Damage-initiation Load Drop**: GNPs reduced the load drop at damage initiation by up to 93% at 2.0 wt.%—the largest and most consistent structural improvement observed—by activating crack deflection, interlayer separation, and frictional energy dissipation in the fracture process zone. The activation of these mechanisms is a recognised signature of enhanced fracture toughness, confirming that the observed load-drop reduction is governed by GNP-mediated toughness improvement. Implying the same, the fracture mode also transitioned from unstable stick-slip to stable distributed cracking.
2. **Enhanced Energy Absorption Capacity**: Absorbed energy capacity improved by up to 17% at 1.0 wt.% ($p=0.014$), driven by GNP-enhanced mode I fracture toughness — a further manifestation of GNP-mediated toughness enhancement. The optimum shifted from 1.5 wt.% (flat-panel tests) to 1.0 wt.% due to intensified filtration-induced re-agglomeration under vacuum consolidation. The understanding that geometry and pressure-difference changes filtration extent within the two fabrication contexts directly bridges coupon-level material characterisation and structural-scale performance, a gap that currently limits the design use of fracture toughness data.
3. **Strain Field Diffusion**: DIC revealed that GNP addition progressively transforms the strain field from concentrated-localised to diffuse-distributed, directly evidencing a broader fracture process zone and consistent with multi-crack energy dissipation — both hallmarks of GNP-mediated toughness enhancement. The DIC provided the first experimental evidence that the fracture process zone in a structural composite joint is a concentration-dependent, engineerable quantity rather than a fixed geometric feature of the joint. The monotonic and quantitatively smooth relationship between GNP content and strain field geometry means that a DIC measurement could also be used to non-destructively verify dispersion quality in a production batch, since poor dispersion would produce a more concentrated field than the nominal concentration.
4. **Mechanism Leading to Monotonic Stiffness Reduction**: Joint stiffness decreased monotonically by up to 36% at 2.0 wt.% due to three coupled mechanisms: (i) incomplete graphene exfoliation resulting in loss of potential graphene-matrix interfacial area and leaving low-stiffness vdW interstices to become eventual load bearers ($C_{33} \approx 38$ GPa, $C_{44} \leq 5$ GPa vs. in-plane 1 TPa), (ii) weak interparticle contact in re-agglomeration during wet layup and vacuum consolidation, and (iii) displacement of stiffer epoxy resin volume with weak vdW interstice as nanoparticle loading increases. The vdW interstice displacement mechanism is intrinsic to platelet geometry. Elucidation of these underlying mechanisms, provides the basis for a modified Halpin-Tsai or Mori-Tanaka model incorporating an interlayer compliance correction, allowing platelet nanocomposites stiffness to be more accurately predicted.
5. **Strength Penalty Above Critical Loading**: Damage initiation load and ultimate strength were significantly reduced above 1.0 wt.%, where agglomerate-induced stress concentration and void sites exceed the benefit of dispersed platelets.
6. **Optimal Concentration and Dispersion Requirements**: The effective concentration window for combined toughness benefit with acceptable stiffness and strength is 0.5–1.0 wt.% for calendar-dispersed xGNP M-25. Achieving graphene's full reinforcement potential in structural T-joints requires GNP pre-exfoliation, chemical functionalisation, surfactant use or manufacturing-compatible high-shear dispersion methods.

7. **Deformation Capacity for Crashworthy Joints**: The significant 23% increase in displacement at ultimate load at 1.0 wt.% is a finding allowing GNP use in secondary load-redistribution joints and crash-energy-absorbing substructures (the fuselage keel frames, underfloor connections, and window-belt joints), needing to sustain substantial deformation before complete separation as the defining requirement for crashworthy substructures.

From these results, three important implications follow for structural composite design: (1) GNPs at 0.5–1.0 wt.% provide net toughness benefit (reduced load drop, increased AEC) with acceptable stiffness reduction (<16%), making this regime viable for damage-tolerant aerospace joints. (2) The benefit ceiling is graphene de-stacking limited and rather than being governed solely by agglomeration. Processing that enhances mono layer graphene isolation and suppresses agglomeration will extend the benefit ceiling. (3) Calendaring alone is insufficient for stiffness improvement; chemical functionalisation, surfactant aide or scalable high-shear methods are required for full property exploitation.

5. ACKNOWLEDGEMENTS

This research was funded by the Australian Research Council Discovery Program (DP140100788). One author (M.B.) thanks RMIT University for a PhD scholarship. Gratitude is expressed to Professor Kate Fox and Scientia Professor Chun Wang (UNSW) for facilitating the doctoral thesis completion from which the current work originates. The author gratefully acknowledges Professor Chun Wang (UNSW) and Professor Anthony Kinloch (Imperial College London) for their comments on an earlier version of this paper. Technical assistance from Paul Muscat, Peter Tkatchyk, Julian Bradler, Phil Francis, and Dr Matthew Field is gratefully acknowledged.

6. Contact Author Email Address

Contact author email address mailto: mukesh.bhasin@rmit.edu.au

7. Copyright Statement

The authors confirm that they, and/or their company or organization, hold copyright on all of the original material included in this paper. The authors also confirm that they have obtained permission, from the copyright holder of any third-party material included in this paper, to publish it as part of their paper. The authors confirm that they give permission or have obtained permission from the copyright holder of this paper, for the publication and distribution of this paper as part of the ICAS proceedings or as individual off-prints from the proceedings.

References

[1] May M, Ganzenmüller G, Wolfrum J, Heimbs S. Analysis of composite T-joint designs for enhanced resistance to hydrodynamic ram. Composite Structures. 2015;125:188–94.
[2] Eaton DCG, Slachmuylders EJ. The use of advanced materials in space structure applications. Acta Astronautica. 1988;17:863–74.
[3] Mouritz A. Introduction to Aerospace Materials. Introduction to Aerospace Materials. Washington, DC: Woodhead Publishing Reston, VA : Cambridge, UK; 2012. p. 428–53.
[4] Heimbs S, Nogueira AC, Hombergsmeier E, May M, Wolfrum J. Failure behaviour of composite T-joints with novel metallic arrow-pin reinforcement. Composite Structures. 2014;110:16–28.
[5] Thawre MM, Pandey KN, Dubey A, Verma KK, Peshwe DR, Paretkar RK, et al. Fatigue life of a carbon fiber composite T-joint under a standard fighter aircraft spectrum load sequence. Composite Structures. 2015;127:260–6.
[6] Dutton S, Kelly D, Baker A. Composite Materials for Aircraft Structures, Second Edition. Reston ,VA: American Institute of Aeronautics and Astronautics; 2004.
[7] Greenhalgh ES. Delamination-dominated failures in polymer composites. Failure Analysis and Fractography of Polymer Composites: Woodhead Publishing Limited; 2009. p. 1–595.
[8] Hasan Z, Chattopadhyay A, Liu Y. Multiscale Approach to Analysis of Composite Joints Incorporating Nanocomposites. Journal of Aircraft. 2015;52:204–15.
[9] Hallander P, Petersson M, Weidmann B, Grankall T, Strindberg G, Pontus N. Nano-Reinforced Radius Filler For An Aircraft Structure And A Method Of Producing An Aircraft Structure Comprising Such Filler. United States Patent and Trademark Office; 2012.

[10] West System Inc. West System 105 Resin Engineering Data Sheet. ATL Composites Pty Ltd; 2017.
[11] West System Inc. 105 Epoxy Resin /206 Slow Hardener Technical Data Sheet. West System; 2014.
[12] XG Sciences Inc. xGNP® Graphene Nanoplatelets Material Safety Data Sheet. East Lansing, Michigan: XGSciences; 2010. p. 1–6.
[13] Chatterjee S, Nafezarefi F, Tai NH, Schlagenhauf L, Nüesch FA, Chu BTT. Size and synergy effects of nanofiller hybrids including graphene nanoplatelets and carbon nanotubes in mechanical properties of epoxy composites. Carbon. 2012;50:5380–6.
[14] Gong L, Kinloch IA, Young RJ, Riaz I, Jalil R, Novoselov KS. Interfacial stress transfer in a graphene monolayer nanocomposite. Advanced Materials. 2010;22:2694–7.
[15] Spanu L, Sorella S, Galli G. Nature and Strength of Interlayer Binding in Graphite. Physical Review Letters. 2009;103.
[16] Ahmadi-Moghadam B, Taheri F. Fracture and toughening mechanisms of GNP-based nanocomposites in modes I and II fracture. Engineering Fracture Mechanics. 2014;131:329–39.
[17] Bhasin M, Wu S, Ladani RB, Kinloch AJ, Wang CH, Mouritz AP. Increasing the fatigue resistance of epoxy nanocomposites by aligning graphene nanoplatelets. International Journal of Fatigue. 2018;113:88–97.
[18] Ahmadi-Moghadam B, Taheri F. Influence of graphene nanoplatelets on modes I, II and III interlaminar fracture toughness of fiber-reinforced polymer composites. Engineering Fracture Mechanics. 2015;143:97–107.
[19] Ravindran AR, Ladani RB, Wang CH, Mouritz AP. Hierarchical mode I and mode II interlaminar toughening of Z-pinned composites using 1D and 2D carbon nanofillers. Composites Part A: Applied Science and Manufacturing. 2019;124:105470.
[20] Jia Z, Feng X, Zou Y. An investigation on mode II fracture toughness enhancement of epoxy adhesive using graphene nanoplatelets. Composites Part B: Engineering. 2018;155:452–6.
[21] Young RJ, Kinloch IA, Gong L, Novoselov KS. The mechanics of graphene nanocomposites: A review. Composites Science and Technology. 2012;72(12):1459–76.
[22] Liu Z, Liu JZ, Cheng Y, Li Z, Wang L, Zheng Q. Interlayer binding energy of graphite: A mesoscopic determination from deformation. Physical Review B - Condensed Matter and Materials Physics. 2012;85:1–5.
[23] Benedict LX, Chopra NG, Cohen ML, Zettl A, Louie SG, Crespi VH. Microscopic determination of the interlayer binding energy in graphite. Chemical Physics Letters. 1998;286(5-6):490–6.
[24] Anagnostopoulos G, Androulidakis C, Koukaras EN, Tsoukleri G, Polyzos I, Parthenios J, et al. Stress transfer mechanisms at the submicron level for graphene/polymer systems. ACS Applied Materials and Interfaces. 2015;7:4216–23.
[25] U.S. Department of Transportation Federal Aviation Administration. 20-107B - Composite Aircraft Structure. USA2009.
[26] Federal Aviation Administration. AC: 20-107B - Composite Aircraft Structure Change 1. 2009.
[27] Bhasin M. Graphene reinforced aerospace polymer composites with improved toughness and damage tolerance.: RMIT University; 2023.
[28] Prolongo SG, Moriche R, Jiménez-Suárez A, Sánchez M, Ureña A. Advantages and disadvantages of the addition of graphene nanoplatelets to epoxy resins. European Polymer Journal. 2014;61:206–14.
[29] Blakslee OL, Proctor DG, Seldin EJ, Spence GB, Weng T. Elastic constants of compression-annealed pyrolytic graphite. Journal of Applied Physics. 1970;41:3373–82.
[30] Savini G, Dappe YJ, Öberg S, Charlier JC, Katsnelson MI, Fasolino A. Bending modes, elastic constants and mechanical stability of graphitic systems. Carbon. 2011;49:62–9.
[31] Peterlik H, Paris O, Young RJ, Sun Y, Hartmann MA, Todt M, et al. Structure and Multiscale Mechanics of Carbon Nanomaterials. Leoben, Austria: Springer 2016.
[32] Shen Y, Wu H. Interlayer shear effect on multilayer graphene subjected to bending. Applied Physics Letters. 2012;100:1–4.
[33] Zhang YY, Wang CM, Cheng Y, Xiang Y. Mechanical properties of bilayer graphene sheets coupled by sp3 bonding. Carbon. 2011;49:4511–7.
[34] Wang G, Liu L, Zhang Z. Interface Mechanics in Carbon Nanomaterials-based Nanocomposites. Composites Part A: Applied Science and Manufacturing. 2020;141:106212.

[35] Bosak A, Krisch M, Mohr M, Maultzsch J, Thomsen C. Elasticity of single-crystalline graphite: Inelastic x-ray scattering study. Physical Review B - Condensed Matter and Materials Physics. 2007;75:1–4.
[36] Michel KH, Verberck B. Theory of the elastic constants of graphite and graphene. Physica Status Solidi (B) Basic Research. 2008;245:2177–80.
[37] Lee C, Wei X, Kysar JW, Hone J. Measurement of the Elastic Properties and Intrinsic Strength of Monolayer Graphene. Science. 2008;321:385–8.